Materials Research Express

PAPER • **OPEN ACCESS**

Fabrication and characterization of TiOx based single-cell memristive devices

To cite this article: Bünyamin Özkal *et al* 2023 *Mater. Res. Express* **10** 125901

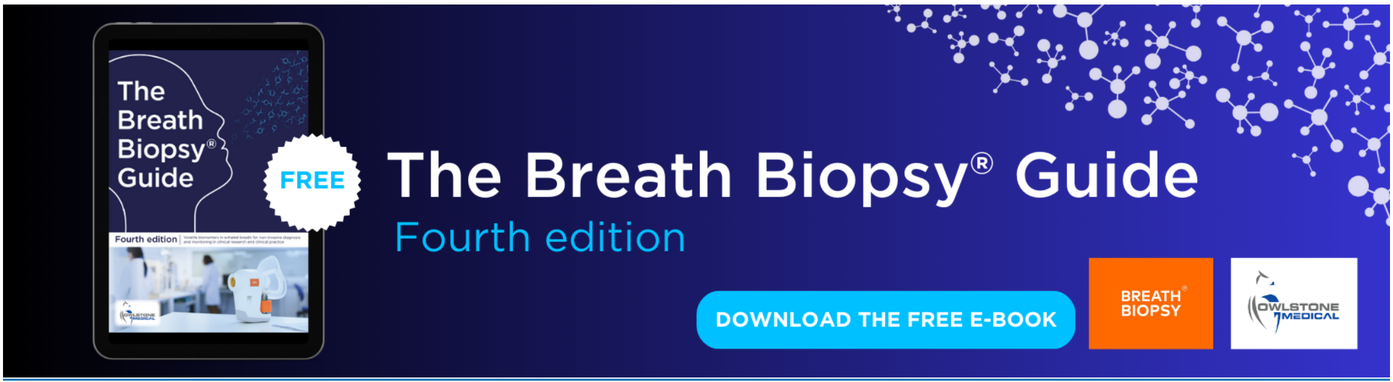

IOP Publishing *Mater. Res. Express* **10** (2023) 125901 https://doi.org/10.1088/2053-1591/ad1125

Materials Research Express

OPEN ACCESS

RECEIVED
21 August 2023

REVISED
7 November 2023

ACCEPTED FOR PUBLICATION
30 November 2023

PUBLISHED
12 December 2023

PAPER

Fabrication and characterization of TiOx based single-cell memristive devices

Bünyamin Özkal[1], Sinan Kazan[1,*], Özgül Karataş[1,2], Gökhan Ekinci[1,3], Lütfi Arda[4] and Bulat Z Rameev[1,5,6]

[1] Department of Physics, Gebze Technical University, Kocaeli, Turkey
[2] Department of Electrical and Energy, Konya Technical University, Konya, Turkey
[3] Faculty of Science and Letters, Pîrî Reis University, Tuzla, Istanbul, Turkey
[4] Mechatronics Engineering Department, Bahçeşehir University, Istanbul, Turkey
[5] Kazan State Power Engineering University, 420066 Kazan, Tatarstan, Russia
[6] E. Zavoisky Physical-Technical Institute, FRC Kazan Scientific Center of RAS, 420029 Kazan, Tatarstan, Russia
[*] Author to whom any correspondence should be addressed.

E-mail: kazan@gtu.edu.tr

Keywords: memristor, resistive switching, generalized memristor model, TiO2, PLD, XPS, PL

Abstract

Nowadays, remarkable progress has been observed in research into neuromorphic computing systems inspired by the human brain. A memristive device can behaviorally imitate the biological neuronal synapse therefore memristor-based neuromorphic computing systems have been proposed in recent studies. In this study, the memristive behaviors of titanium dioxide sandwiched between two platinum electrodes were investigated. For this purpose, three $SiO_2/Pt/TiO_x/Pt$ thin films with 7.2 nm, 40 nm, and 80 nm TiO_x metal-oxide layers were fabricated using a pulsed laser deposition technique. The fabrication process, structural properties, photoluminescence properties and electrical transport characterization of each thin film have been investigated. All thin films were analyzed in terms of the film stoichiometry and degree of oxidation using high-resolution x-ray photoelectron spectroscopy. By measuring the layer thickness, density, and surface roughness with the x-ray reflectivity technique, by analyzing the structural defects with photoluminescence spectroscopy and by characterizing the quasi-static electrical properties with the conventional two probes technique, we have shown that the fabricated memristive devices have bipolar digital switching properties with high R_{OFF}/R_{ON} ratio. This type of switching behavior is applicable in random access memories. Experimental current–voltage behavior in the form of pinched hysteresis loop of the films have been modelled with generalized memristor model.

1. Introduction

Analyzing the known three basic passive circuit elements of electronics, such as a capacitor, resistor, and inductor, in 1971 Leon Chua [1] formulated six mathematical relationships between the four circuit variables: electric current (i), voltage (v), electric charge (q), and flux (φ). Using the symmetry arguments of these mathematical relationships, Chua envisioned the new dynamic circuit element called a Memory-Resistor or simply Memristor as a fourth passive element relating charge and flux. In 2008 a group at Hewlett-Packard (HP) Lab announced that the sandwich structure consisting of TiO_2 thin film between two platinum electrodes provides a memristive switching behavior [2]. This new experimental result has led to the attention of many disciplines such as information processing technologies [3–5], CMOS circuit design [6–8], random access memory technologies [9, 10], artificial neural networks [11–15], as well as many scientific communities such as electronics, material, physics, chemistry, biology to this new passive circuit element. A memristor device in the form of a nano-scaled Metal/Metal-Oxide/Metal (MIM) thin film structure is a two-terminal circuit element driven by an external stimulus (current or voltage). Since the electrical resistance of the device changes with the amount of charge flowing through the device, it exhibits a non-linear current–voltage characteristic [2]. Chua proved that this behavior cannot be produced with only the other three basic circuit elements, so the memristor has been accepted as a new fundamental circuit element [1, 16]. Due to the hysteretic behavior of the current–voltage curve, the device is named as memristor which combines the names of 'resistance' and 'memory' because the device remembers its previous resistance state [1]. This functionality of the device shows that it can be used as a memory element in CMOS technology in the future. Furthermore, when used with a transistor in hybrid CMOS chip circuits, it has the potential to enhance device performance [17]. With its low power consumption, scalability, and controlled voltage-current feature, it can serve as a biological synapse in real brain-like processors [18, 19].

The first memristor model proposed by HP is explained by the linear drift of positively charged oxygen vacancies in TiO_2 oxide driven by an external electric field [2]. During the electroforming process of the $Pt/TiO_2/Pt$ device, a conductive filament where oxygen vacancies are much more abundant than in other regions, is formed in the TiO_2 insulator. At this stage, even though a conductive filament is formed between the two metal electrodes, the device has a high electrical resistance due to the insulating region, and the resistance state of the entire device is named as High Resistance State (HRS or OFF state). When the electric field applied between the two metal electrodes is large enough, the oxygen vacancies start to drift toward the opposite metal electrode, causing an abrupt increment in the device's conductivity and the growth of the filament structure (SET state). After the SET process, the filament structure nearly connects the two metal electrodes, causing the resistance state of the entire device to change from a high resistance state to a low resistance state which is called as LRS (or ON) state. When the polarity of the applied voltage is reversed and the voltage is large enough, the opposite electric field causes the conductive filament to dissolve and a sudden drop occurs in conductivity (RESET), causing the entire device to return from the low resistance state (ON state) to the high resistance state (OFF state).

Since the realizing of the first $Pt/TiO_2/Pt$ memristor device by HP Lab. many memristor devices with different structure and different materials [20–24] have been investigated. This variety in the field of memristors led to the development of different memristor models to explain the current–voltage characteristic in the form of a pinched-hysteresis loop [25–32]. These models help to understand the behavior of devices under different stimuli just as a sinusoidal, triangular or square pulse with different time and it is possible to extract some device characteristics. In addition to the mathematical model a physical model based on the Simmons tunneling effect in Metal/Insulator/Metal structure has been investigated [33]. The generalized memristor model [32] based on the other mathematical and physical models have been used in literature to simulate the I-V curve more accurately and it is possible to extract the memristors parameters.

Generally, memristor devices consist of binary metal oxide dielectric such as TiO_2 [34, 35], SiO_2 [36], Al_2O_3 [37], HfO_2 [38], CuO [39, 40], NiO [41–43], ZnO [44]. The resistive switching phenomenon between two conduction states has been observed in a wide variety of transition metal oxides, such as PCMO [45], $SrZrO_3$ [46], and $SrTiO_3$ [47]. However, the observed switching behavior strongly depends on the material type. There is steadily increasing research interest in the various memristor concepts to realize lower power, higher nonlinearity, bipolar and faster switching mechanisms.

The hysteretic behavior of the current–voltage curve of metal-oxide memristor devices makes it possible to use as a memory device. Unlike conventional random-access memories, memristor-based memory devices are nonvolatile [48]. The electrical characteristics of the memristor devices strongly depend on their design and fabrication technique. Therefore SET / RESET process shows variation from device to device or from cycle to cycle. These properties have been adapted for security applications, such as random number generators [49, 50]. In addition to a non-volatile memory application, memristors have already found applications in neuromorphic computation circuits due to the multiple resistance states [51]. Another prominent characteristic of the memristors is their ability to mimic so-called spike-timing-dependent plasticity (STDP) which is important to realize the neural synaptic learning mechanism. [52, 53]. Moreover, they can be also used in the implementation of Event-Driven neural systems [54]. Thus, neuromorphic computation science/technology based on memristor-CMOS learning systems attract the increasing attention of researchers.

Since the renaissance of real memristor device, TiO_2 binary oxide material have been studied as a prototype material for many memristor research community. In this work, the memristive behavior of the single cell consisting of titanium-oxide (TiO_x) layer between Pt electrodes grown on SiO_2 substrate by PLD technique has been investigated. Possibility to control the parameters of PLD parameters (vacuum pressure, substrate temperature, etc) gives an advantage of tailoring the stoichiometry, oxygen vacancy concentration and other structural and electrophysical properties of TiO_x layers. The structural properties and the stoichiometry of the grown films have been characterized by x-ray reflectivity technique and x-ray photoelectron spectroscopy. Defect energy level in band gap and optical activities of the TiO_x have been measured by using photoluminescence method. DC electrical characterization of the stacked $SiO_2/Pt/TiO_x/Pt$ thin films have been measured in order to observe memristive behaviors. We have shown that bipolar switching of both digital

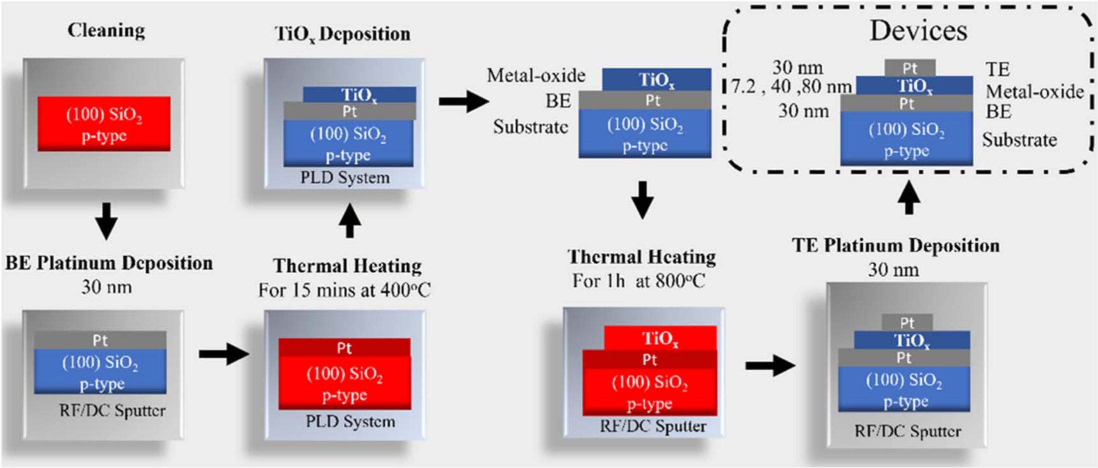

Figure 1. Fabrication process of the single-cell TiO_x based memristor device.

and analog switching behavior can be obtained depending on the sample thickness. Furthermore, we have demonstrated that the generalized memristor model can be applied to our structures to simulate the experimental results and help in fabrication of the device with desirable parameters.

2. Materials and method

Single-cell memristor device in the form of $SiO_2/Pt/TiO_x/Pt$ stacked thin films were grown in high vacuum chambers with different oxide thicknesses as shown in figure 1. Before the growing process, the 10 mm × 10 mm sized SiO_2 (100) substrates were ultrasonically cleaned in acetone, isopropanol and distilled water for 5 min successively and heated for 15 min at 400 °C for thermal cleaning. Initially, SiO_2 substrates were coated with 30 nm platinum (Pt) as a bottom electrode (BE) in an RF/DC magnetron sputter chamber at $\sim 10^{-9}$ mbar (UHV) base pressure. In the device fabrication process, after growing the bottom Pt electrode we took the sample out of the chamber to prepare the contact region and then it was replaced in the vacuum chamber. Before being placed in a vacuum chamber again, it was cleaned in acetone, isopropanol, and distilled water for 5 min respectively and heated for 15 min at 400 °C for thermal cleaning.Then, the sample was transferred to the pulsed laser deposition (PLD) chamber for TiO_x metal-oxide layer deposition. RF/DC magnetron sputter chamber and PLD chamber are connected to each other through a connection system that maintains to the vacuum conditions. In the PLD process, a KrF excimer laser ($\lambda = 248$ nm) source with a repetition rate of 10 Hz was applied to TiO_2 PLD targets. The laser beam from the pulsed KrF excimer laser was focused on the TiO_2 target at a 45° incidence angle through the spherical lens and the laser energy density on the target was about 2.4 J cm^{-2}. The growth temperature was fixed at room temperature and the background pressure was kept at $\sim 1.0 \times 10^{-8}$ mbar. The distance from the substrates to the target was set as 34 mm. All PLD parameters were kept constant, and all substrates were rotated at a low speed during the deposition. TiO_x thin film has been grown by using a TiO_2 PLD target. To increase the growth quality and number of oxygen vacancies in the oxide layer of $SiO_2/Pt/TiO_x$ thin films, they were annealed at 800 °C for 1h in $\sim 1 \times 10^{-9}$ mbar vacuum condition. XPS measurements show that the oxygen vacancies were generated at the surface after thermal treatment. Finally, $SiO_2/Pt/TiO_x$ substrates were coated with platinum (Pt) as a top electrode (TE) under the same conditions as the bottom electrode. By using the same condition $SiO_2/Pt/TiO_x/Pt$ devices with thickness of 7.2 nm, 40 nm, and 80 nm TiO_x thin films were fabricated. The surface area of the top electrode is about 1 mm × 1mm square region.

The thickness, physical density, and interlayer surface roughness of the bottom/top electrode and metal oxide layer in the produced films were determined very precisely using the small angle x-ray Reflectivity (SA-XRR) technique using Rigaku XRD device with CuKa x-ray source ($\lambda = 0.154$ nm) at room temperature.

The stoichiometry and the oxidation degree of the elements in oxide material for all thin films were analyzed by x-ray Photoelectron Spectroscopy (XPS) method. The XPS measurements were carried out using an Al Kα radiation (hv = 1486.6 eV) and a hemispherical electron analyzer (Phoibos 100, SPECS GmbH, Berlin, Germany) at room temperature. During the measurements base pressure of XPS chamber was fixed at about $\sim 10^{-9}$ mbar. To obtain the chemical bonding energies by simulating to the experimental results, fitting with Gaussian/Lorentzian peak was used after subtracting the Shirley-type background at CasaXPS software [55].

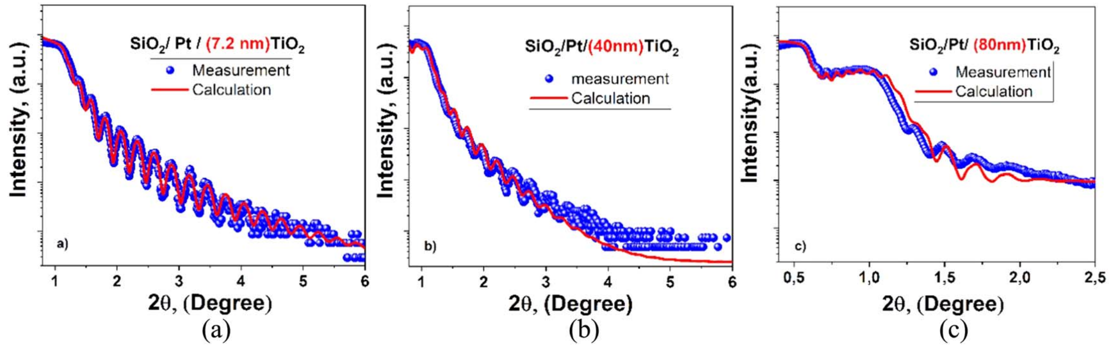

(a) (b) (c)

Figure 2. The small-angle x-ray Reflectivity (XRR) results of $SiO_2/Pt/TiO_x$ thin films with 7.2 nm (a), 40 nm (b), and 80 nm TiO_x (c) metal-oxide layers (The red line represents to the simulation and the blue-solid circle shows the of experimental data).

Table 1. The estimated layer thickness, density and the roughness of each layer in the sample stack for three different samples.

Sample	7.2 nm TiO_2			40 nm TiO_2			80 nm TiO_2		
Layers	SiO_2	Pt	TiO_2	SiO_2	Pt	TiO_2	SiO_2	Pt	TiO_2
Roughness (nm)	0.58	—	—	0.95	—	—	0.29	—	—
Thickness (nm)	173	30	**7.2**	200	30	**40**	216	30	**80**
Density (gr/cm^3)	2.2	21.45	4.23	2.2	21.45	4.23	2.2	21.45	4.23

The photoluminescence (PL) measurements were performed on the samples using Agilent Cary Eclipse Fluorescence Spectrophotometer at room temperature.

Quasi-static DC electrical characterizations of memristor devices were measured with the conventional two probes of the four-point probe technique at room temperature using Keithley 2400 SourceMeter and current -voltage (I-V) program via LabVIEW software.

3. Results and discussion

3.1. XRR results

X-ray Reflectivity (XRR) measurements have been done by using a Rigaku XRD device. The obtained results have been simulated with Rigaku GlobalFit software at Institute of Nanotechnology at GTU. Processing has been carried out in a parallel beam of 5 mm slit width and XRR $\theta-2\theta$ degree scans have been recorded within the angular range from 0 to 6 degrees and have been focused on related data on the graphics. The critical angles of the order of 1—1.1 has been observed for all sample. Figure 2 shows the XRR curves and the best-fitting of these curves with suitable parameters for three different samples. The fitting parameters of each layer as the thickness, density, and surface roughness of the $SiO_2/Pt/TiO_x/Pt$ films are listed in table 1. The thickness of the TiO_x oxide layer is estimated as 7.2, 40 and 80 nm. These values are consistent with the growth conditions such as frequency and duration of pulsed laser in the PLD system. The physical density of the TiO_x material has been taken as 4.23 gr/cm^3 which is the bulk rutile TiO_2 value [56].

3.2. XPS results

X-ray photoelectron spectroscopy (XPS) is a general non-destructive technique to provide sensitive and remarkable information about the chemical composition and electronic structure of the surface. Moreover, elemental composition and the formation of chemical bonds between components of metal oxide are investigated with the XPS method. In this study the stoichiometry and the oxidation degree of constitute elements were analyzed by considering the Ti 2p and O 1s core energy levels with high-resolution XPS (Phoibos 100, SPECS GmbH, Berlin, Germany). Figure 3 shows the high-resolution XPS spectra of the thermally annealed and non-annealed TiO_x thin film as well as the simulation of experimental XPS spectra with CasaXPS software [55]. The measured Ti_{2p} doublet peaks arising from the spin–orbit coupling were simulated considering to the Ti^{4+}, Ti^{3+}, Ti^{2+} and Ti°. All fitting parameters are presented in table 2.

As seen in figure 3(a), (a) broad doublet peak of Ti^{x+} with a shoulder was observed. The peak positions of Ti^{x+} $2p_{3/2}$ and $2p_{1/2}$ of non-annealed TiO_x (7.2 nm) film are 459.3 and 464.5 eV respectively. The corresponding

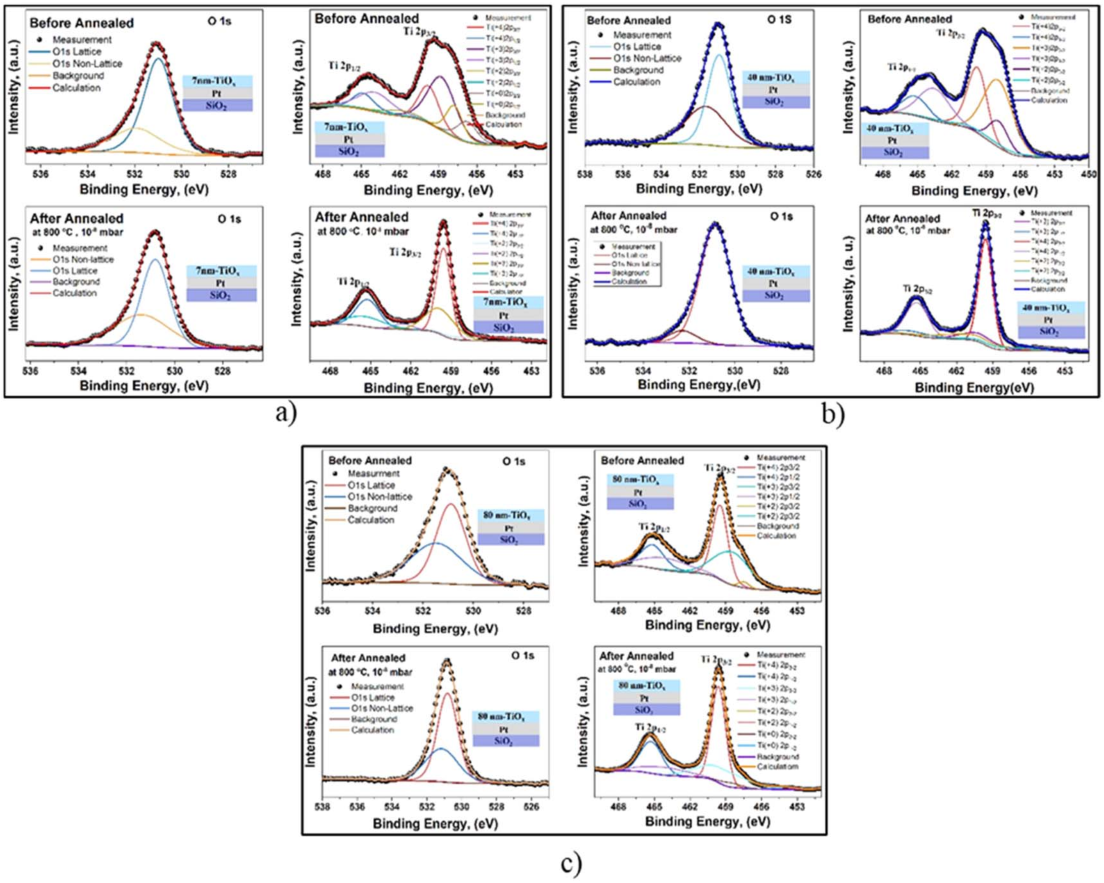

Figure 3. XPS spectra of O_{1s} and Ti_{2p} for thermally annealed and non-annealed TiO_x thin films and the simulation results of the experimental data. (a) Shows the XPS results of annealed and non-annealed $SiO_2/Pt/TiO_x$ (7.2 nm). (b) Shows the XPS results of annealed and non-annealed $SiO_2/Pt/TiO_x$ (40 nm). (c) Shows the XPS results of annealed and non-annealed $SiO_2/Pt/TiO_x$ (80 nm).

spin–orbit coupling energy is measured as 5.2 eV at room temperature. After thermal annealing the peak positions of Ti^{x+} $2p_{3/2}$ and $2p_{1/2}$ are shifted to the 459.57 and 465.23 eV and the corresponding spin–orbit coupling energy was measured as 5.66 eV. According to the simulation results, there are contributions of Ti^{4+}, Ti^{3+}, Ti^{2+} and Ti° to the resultant envelope XPS curve. The ratio of Ti^{+4} has increased from 22% to 87% as the result of thermal treatment at vacuum and these peaks are consistent with Ti^{4+} in TiO_2. On the other hand, the ratio of Ti^{+3} and Ti^{+2} decreased from 44% to 9.3% and 17.7% to 2.6% respectively. These Ti^{+3} and Ti^{+2} ions have been attributed to the broken bonds at the surface and oxygen deficiency in the deeper layer [57]. According to the best fitting of the O_{1s} spectrum this peak was attributed to the lattice and non-lattice oxygen with a binding energy of 530.8 and 531.41 eV, respectively. These results were consistent with experimental data published in the literature [58].

In the literature there are many experimental results showing the TiO_x film from the TiO_2 target as can be seen in References of [59–64]. In these studies, the oxygen vacancy formation on the surface have been attributed to the reconstruction of the surface due to oxygen-deficient atmosphere, such as under vacuum conditions. The reduction of oxygen on the surface of grown film is much higher than the deeper region of the film. Due to the heating of film under vacuum condition reduction of oxygen (oxygen vacancies) can diffuse into the deeper regions of the film. Figure 3 shows the measured XPS data. After annealing of all films, simulation of the data shows to the existence of Ti^{+3} and less Ti^{+2} and this valency has been attributed to the reduction of TiO_2 in to the TiO_x. These results have been supported by Photoluminescence (PL) measurements as seen in figure 4. The main defect states of nanostructured TiO_2 are self-trapped excitons (STE), single ionized oxygen vacancies (Vo^*), doubly ionized oxygen vacancies (Vo^{**}), and excited states of Ti^{3+} at 416 nm, 443 nm, 531 nm and 802 nm, respectively [65–70]. As can be seen form the figure 4 we observed excitation at 416 nm, 443 nm, 531 nm referring to the oxygen vacancies after thermal treatment under vacuum conditions.

3.3. Photoluminescence (PL) results

Photoluminescence (PL) spectra are generally used to study the optical activity, crystal imperfection, impurities and defect density of semiconductor materials. Therefore, photoluminescence measurements were performed

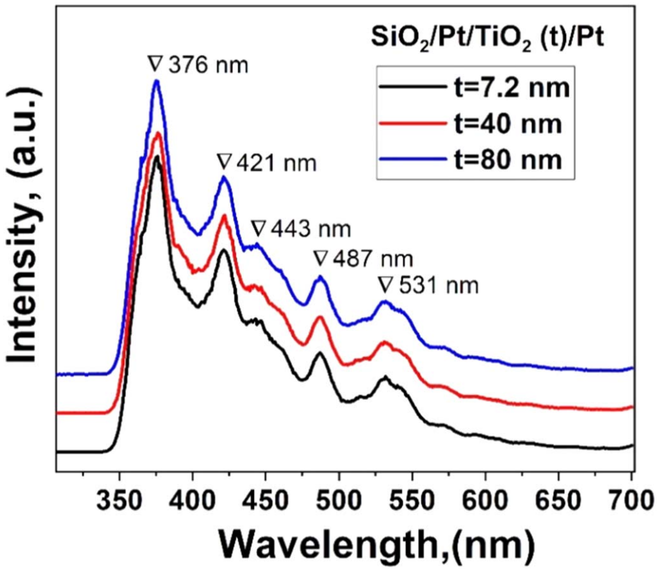

Figure 4. Photoluminescence spectra of $SiO_2/Pt/TiO_2$ thin film with different thicknesses.

Table 2. XPS fitting parameters of $SiO_2/Pt/TiO_x$ (7.2 nm, 40 nm, 80 nm).

SiO_2/Pt(30 nm)/TiO_2(7.2 nm)							
7.2 nm TiO_2 Non-annealed	**2p3/2** BE(eV)	**2p1/2** BE(eV)	**Gap** (eV)	**7.2 nm TiO_2** Annealed(800 °C)	**2p3/2** BE(eV)	**2p1/2** BE(eV)	**Gap** (eV)
Ti(0)	456.8	461.5	4.7	**Ti(0)**	—	—	—
Ti(+2)	457.8	462.3	4.5	**Ti(+2)**	457.9	462.6	4.7
Ti(+3)	458.9	465	6.1	**Ti(+3)**	460	465.6	6.6
Ti(+4)	**459.3**	**464.5**	**5.2**	**Ti(+4)**	**459.57**	**465.23**	**5.66**
	O1s BE(eV)				**O1s BE(eV)**		
Lattice	531			**Lattice**	530.8		
Non-Lattice	531.9			**Non-Lattice**	531.4		
SiO_2/Pt(30 nm)/TiO_2(40 nm)							
40 nm TiO_2 Non-annealed	**2p3/2** BE(eV)	**2p1/2** BE(eV)	**Gap** (eV)	**40 nm TiO_2** Annealed(800 °C)	**2p3/2** BE(eV)	**2p1/2** BE(eV)	**Gap** (eV)
Ti(0)	—	—	—	**Ti(0)**	—	—	—
Ti(+2)	458	462.1	4.1	**Ti(+2)**	457.5	462.2	4.7
Ti(+3)	458.1	463.7	5.6	**Ti(+3)**	460.5	465.8	5.3
Ti(+4)	459.9	465.3	5.4	**Ti(+4)**	459.59	465.29	5.7
	O1s BE(eV)				**O1s BE(eV)**		
Lattice	530			**Lattice**	530.9		
Non-Lattice	531.7			**Non-Lattice**	532.3		
SiO_2/Pt(30 nm)/TiO_2(80 nm)							
80 nm TiO_2 Non-annealed	**2p3/2** BE(eV)	**2p1/2** BE(eV)	**Gap** (eV)	**80 nm TiO_2** Annealed(800 °C)	**2p3/2** BE(eV)	**2p1/2** BE(eV)	**Gap** (eV)
Ti(0)	—	—	—	**Ti(0)**	454.4	458.4	4
Ti(+2)	457.5	462.2	4.7	**Ti(+2)**	457.7	463.3	5.6
Ti(+3)	458.7	463.9	5.2	**Ti(+3)**	458.9	464	5.1
Ti(+4)	459.5	465.2	5.7	**Ti(+4)**	459.6	465.3	5.7
	O1s BE(eV)				**O1s BE(eV)**		
Lattice	530.9			**Lattice**	530.8		
Non-Lattice	531.5			**Non-Lattice**	531.2		

to investigate the effect of film thickness on the photoluminescence properties of TiO_x metal-oxide layers. Figure 4 presents the results of Photoluminescence measurements at room temperature for different thicknesses TiO_x thin film on SiO_2 substrate. All samples were stimulated with a 275 nm wavelength laser beam by Agilent Cary Eclipse Fluorescence Spectrophotometer.

As shown in figure 4 the peaks of TiO_x films for three different thicknesses overlap with a slight difference. For all samples five mean peaks centered at 376 nm, 421 nm, 443 nm 487 nm and 531 nm were observed as

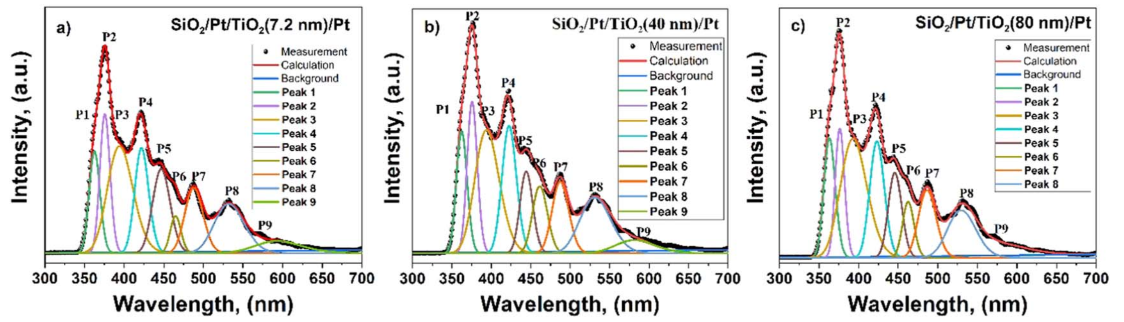

Figure 5. Gaussian decompositions of photoluminescence spectra of the TiO_x films at (a) 7.2 nm, (b) 40 nm, and (c) 80 nm.

similar to the results was reported by Mathew *et al* [71]. Among the peaks forming the spectrum, the 387 nm wavelength is defined as excitonic emission, and the other peaks are defined as surface state emissions [72]. However, as seen in figure 4, the sub-peaks are not clearly visible, and it is very difficult to get information about the defects-related emission. In the literature, although the defects in TiO_2 films have been extensively studied by researchers, the underlying mechanisms are still not fully defined. For this reason, the source of sub-peaks and defects should be examined in detail.

The photoluminescence spectra of the TiO_x films were subjected to Gauss decomposition to determine the luminescence properties in detail. 'Fityk' software was used to obtain Gaussian decomposition [73]. The spectrum curves model in Gauss decomposition is depicted in figure 5 and fitting parameters are presented in table 3. As seen in figure 5 the nine Gaussian decompositions of photoluminescence spectra were plotted versus emission wavelength for different TiO_x film thicknesses. These peaks have been attributed to the different emissions; two ultraviolet emissions (Peak 1 and Peak 2), two violet emission (Peak 3 and Peak 4), two blue emissions (Peak 5 and Peak 6), three green emissions (Peak 7, Peak 8 and Peak 9). There are two dominant emission peaks one of which was the ultraviolet (Peaks 1 and 2) and the other the visible region (Peaks 3, 4, 5, 6, 7, 8, and 9).

3.4. Electrical characterization and modelling

Initially $SiO_2/Pt/TiO_x/Pt$ stacked devices are at a high resistance (~MΩ) state before the electroforming process. In order to produce memristive behavior some amount of oxygen vacancies have to be created into the TiO_2. By applying external voltage during a definite time, required oxygen vacancy and a conduction filament between two metal electrodes can be created and the high resistance of the devices is lowered to memristive regime (~kΩ). Figure 6(a) shows to the electroforming profile of all samples for a compliance current (I_{cc}) of 1 mA. At a definite voltage level, the current through the device shows an abrupt increment related to the dielectric breakdown voltage of the metal oxide in the device. Breakdown voltage is significantly affected by the thickness of the oxide material. For the samples of $SiO_2/Pt/TiO_x(t)/Pt$ with the thickness of TiO_2 layer such as $t = 7.2$ nm, 40 nm and the 80 nm, the partial breakdown voltages are observed as 1.98 V, 7.4 V and 18.6 V respectively.

In order to show that the characteristic current–voltage curve of the $SiO_2/Pt/TiO_x/Pt$ memristor device in the form of a pinched hysteresis curve, bidirectional DC voltage sweeping was carried out. Keithley 2400 SourceMeter has been used to measure the electrical current–voltage characteristic by using standard two probes of the four-probe measurement technique. Figure 6(b) shows the typical current–voltage measurement of the sample with 7.2 nm TiO_2 thickness. The current was recorded during a voltage scan with a rate of 2 mV s^{-1} between +1.5 V and −1.5 V. Positive 5 V electroforming voltage has been applied to the as-grown device during 1s. So, it is expected that the device is at low resistance state (LRS) due to the forming of filament/s. Then the electrical connection of the device was reversed. Then we applied following voltage sequences: $0V \rightarrow 5V \rightarrow 0V \rightarrow -5V \rightarrow 0V$. Therefore, characteristic current–voltage curve is clockwise. As seen in all figures the current–voltage characteristic exhibits pinched hysteresis and asymmetric switching behavior between low resistance state and high resistance state. By using the maximum and the minimum of the derivative dI/dV, SET to low resistance state under negative voltage and RESET to high resistance state under positive voltage are determined as 1.3 and 1 V respectively. The other important memristor characteristic is R_{OFF}/R_{ON} ratio which is larger for large loop area. For a voltage smaller than SET and RESET voltage this ratio has been calculated as 2 for the sample that has a thickness of 7.2 nm as seen in figure 6(b). Similarly, the other devices have been subjected to the same measurement process. Considering to the electroforming profile given in figure 6(a), the current was recorded during voltage scan with the rate of 2.67 mV s^{-1} between +2 V and −2 V for the device of 40 nm TiOx active layer. The voltage was swept between +5 V and −5V for the device of 80 nm

Table 3. Fitting parameters of PL spectrum of $SiO_2/Pt/TiO_x$ (7.2 nm, 40 nm, 80 nm) thin films.

Peak label	7.2 nm				40 nm				80 nm				Emission range
	Peak FWHM (nm)	Peak height	Peak area (a.u)	Peak center (eV)	Peak FWHM (nm)	Peak height	Peak area (a.u)	Peak center (eV)	Peak FWHM (nm)	Peak height	Peak area (a.u)	Peak center (eV)	—
Peak 1 (389.195 nm)	0.15	76.516	12.2173	3.4200	0.14843	76.8484	12.1419	3.422	0.157509	80.038	13.4194	3.4142	Ultraviolet
Peak 2 (401.51 nm)	0.132	103.303	14.5151	3.3008	0.133631	95.6798	13.6101	3.3024	0.118876	86.4934	0.9448	3.2969	Ultraviolet
Peak 3 (415.02 nm)	0.3	79.1009	25.2601	3.1453	0.289239	77.4981	23.8606	3.1490	0.314481	79.4709	26.6032	3.1566	Violet
Peak 4 (451.33 nm)	0.144	77.8462	11.9325	2.9388	0.15	80.0712	12.785	2.9356	0.15	77.735	12.412	2.9317	Violet
Peak 5 (467.94 nm)	0.16	62.3134	10.6129	2.7762	0.12	51.4907	6.57722	2.7910	0.123654	56.8598	7.4842	2.7817	Blue
Peak 6 (580.97 nm)	0.09	27.4445	2.62924	2.6678	0.12771	42.1717	5.73296	2.6874	0.0992166	37.4046	3.9504	2.6806	Blue
Peak 7 (619.18 nm)	0.13	47.6399	6.59244	2.5426	0.13	45.0476	6.23372	2.5447	0.136474	45.0815	6.5491	2.5509	Green
Peak 8 (651.08 nm)	0.198	36.2873	7.64807	2.3310	0.2	35.1493	7.48304	2.3351	0.183915	31.6234	6.19094	2.3417	Green
Peak 9 (669.35 nm)	0.24392	8.53586	2.21629	2.0912	0.21855	8.21836	1.91191	2.1333	0.307902	8.1779	2.68032	2.1640	Green

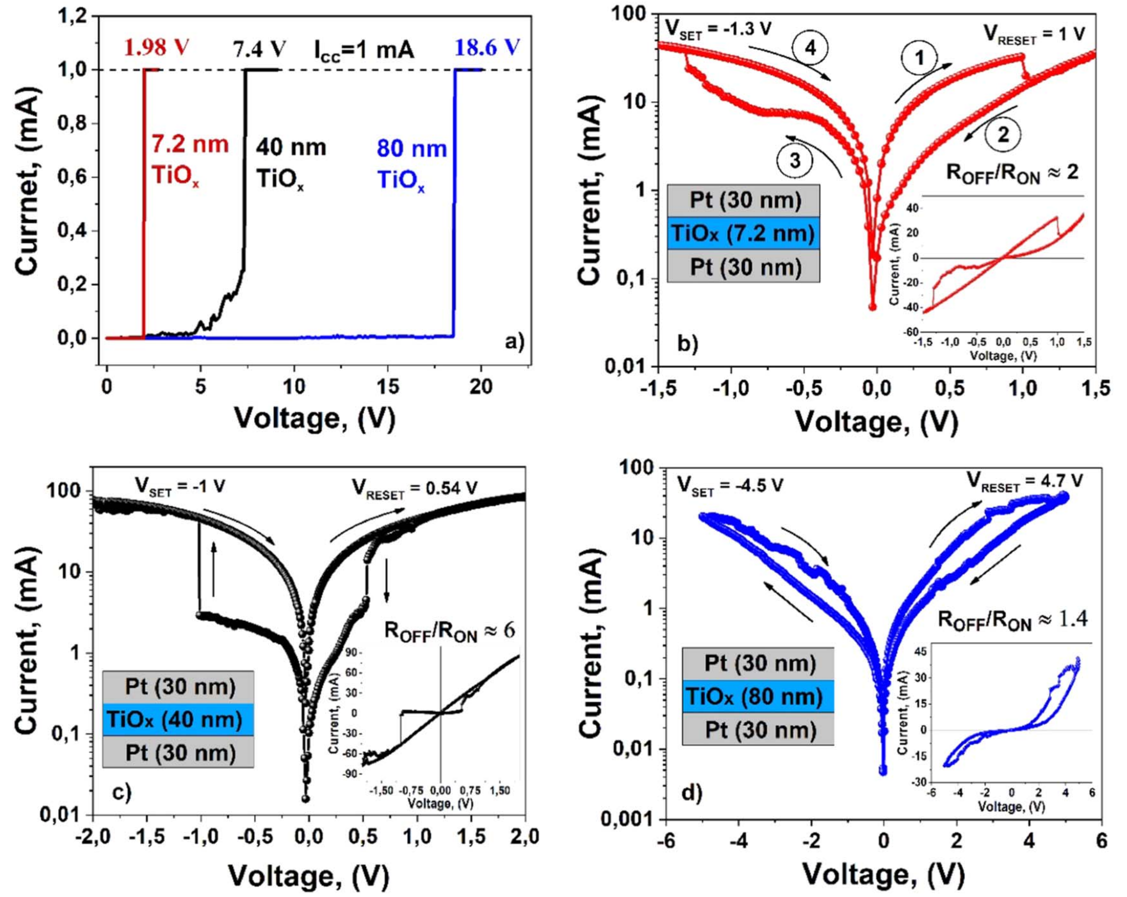

Figure 6. Current–Voltage (I-V) characteristics of the samples. A compliance current of 1 mA is supplied to avoid the breakdown. (a) Forming profile for all devices (b) The I-V curve for the SET and RESET transition for the device of 7.2 nm TiO_x active layer, (c) for the device of 40 nm TiO_x active layer, (d) for the device of 80 nm TiO_x active layer. After applying positive electroforming, initially the device is ON state. Then the polarity of the samples was changed. During the first cycle of the sweeping between ± voltage, the device is in a Low Resistance State (LRS). At a critical positive voltage, the device change from LRS to HRS which is known as the RESET process.

TiOx active layer. Resultant current–voltage characteristics for both samples are given in figures 6(c) and (d). In resistive switching phenomena the variability and reliability of the devices are realized with an endurance test. In characteristic current–voltage measurements the initial endurance of the memristor device has been measured with very high data and drawn only 8 cycles. After eight cycles of measurements the SET voltage is more stable with respect to the RESET voltage. Additionally, the pinched hysteresis loop of the device was observed under AC test with a sinusoidal signal which has an amplitude of 5V and a frequency of 1.6 kHz for one hour. The stable shape of the loop during this measurement is given as an inset figure in figure 7(b).

We have also investigated to the memristive properties of the $SiO_2/Pt/TiO_2$ (40 nm)/Mo sample with DC and AC electrical measurement protocol. The DC measurement has been executed using a Keithley 2400 source-meter at room temperature by DC voltage sweeping between +2V and −2V. Molybdenum (Mo) wire has been utilized as the top electrode while Pt has been used as the bottom electrode for both AC and DC measurement and results are presented in figure 7. Initially, the negative terminal of the external voltage source was connected to the bottom Pt electrode. The measured current values for this sample are lower than the other samples in which Pt thin film is used as the bottom and top electrodes. Also, the loop area of the positive half cycle of the whole hysteresis measurement (Reset switching) is lower than the second half cycle (Set switching). This result has been attributed to the absorption of oxygen ions by the electrochemically active molybdenum electrode [74]. After seven cycle measurements, the SET voltage is more stable with respect to the RESET voltage.

To observe the effect of different electrodes, the molybdenum tip of the measurement system has been used as a top electrode. Then $SiO_2/Pt/TiO_2$ (40 nm)/Mo memristor device was swept with a sinusoidal voltage which has an amplitude of 5V and a frequency of 1.6 kHz. Sinusoidal voltage has been applied by an arbitrary function generator and the current was monitored over a shunt resistor of 1Ω. Experimental setup and measured I-V curve are presented in figure 7(b). In characteristic current–voltage measurements the initial endurance of the memristor device has been measured with very high data and drawn only 8 cycles. After eight cycles of measurements the SET voltage is more stable with respect to the RESET voltage. Additionally, the pinched

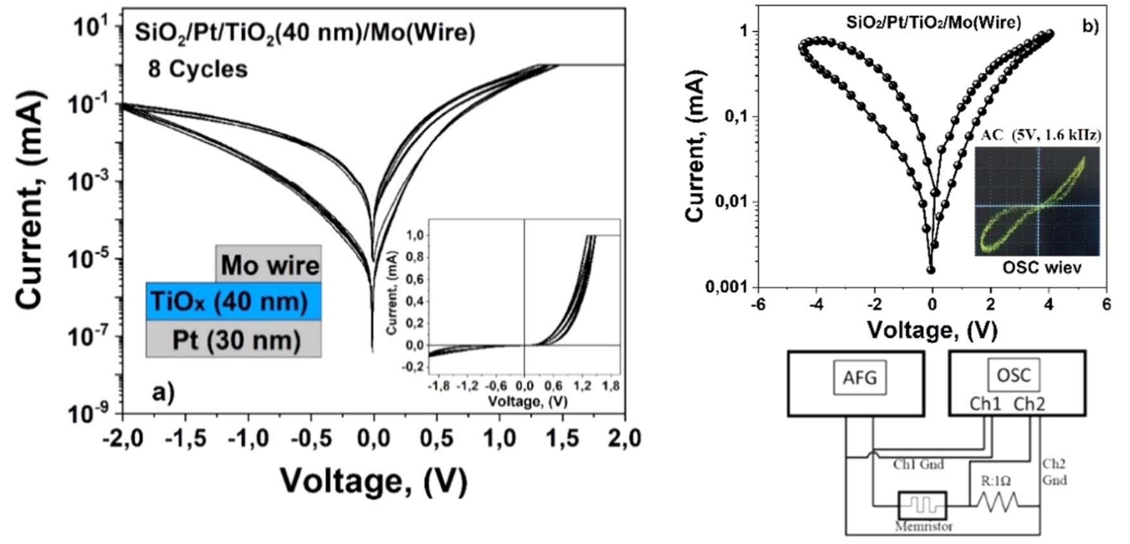

Figure 7. (a) Current–Voltage (I-V) characteristics of the SiO$_2$/Pt/TiO$_2$(40 nm)/Mo(wire) samples under DC swept. The graph is in logarithmic scale and the inset shows the linear scale. (b) Observed I-V curve on an oscilloscope (OSC). A sinusoidal voltage with an amplitude of 5V and a frequency of 1.6 kHz was applied, and the current was monitored over a shunt resistor of 1Ω.

hysteresis loop of the device was observed under AC test with a sinusoidal signal for one hour. The stable shape of the loop during this measurement is given as the inset figure in figure 7(b).

Many memristor devices with different materials and different structures have been investigated due to the increasing interest in the memristive device in the CMOS circuit design [6–8], RAM technology [9, 10] and artificial neural networks [11–15]. Each device has its own memristor characteristic depending on the fabrication technique and structural properties. Therefore, to explain the current–voltage behavior of various memristor devices different mathematical and physical memristor models have been developed. The generalized memristor model [32] based on the other mathematical and physical model have been used to simulate the I-V curve in literature more accurately and it is possible to extract the memristor parameters. The current–voltage relationship based on the quantum tunneling effect in Metal-Insulator-Metal (MIM) junctions proposed by Simmons [33] can be parameterized with a hyperbolic sine function. This relationship is given as

$$i(t) = \begin{cases} a_1 \quad x(t) \quad \sinh(bV(t)), \; V(t) \geqslant 0 \\ a_2 \quad x(t) \quad \sinh(bV(t)), \; V(t) < 0 \end{cases} \tag{1}$$

Due to the nature of the hyperbolic sine function and the increment in the conductivity of the metal oxide, the current increases at a certain threshold voltage value. The parameters b, a_1 and a_2 are used to fit equation (1). It is known from the various memristive device characteristics in the literature that the memristor device's conductivity is higher in the positive voltage region than in the negative region. Therefore, it is understood that different amplitudes of a_1 and a_2 are required depending on the polarity of the applied voltage. Similarly, the parameter b is related to the memristor device's conductivity (the slope of the I-V curve). The HP memristor model [2] is the basis for all proposed memristor models. The position of the boundary between the conductive region (TiO_{2-x}) with excess of oxygen vacancies and the insulating region (TiO_2) is named the state variable ($x(t) = w(t)/D$). This boundary region moves with the applied voltage $V(t)$. As it moves, the memristor device's resistance decreases from its maximum value to its minimum value. Therefore, the shape of the I-V curve (especially the slope) depends on the state variable and its dynamic. Unlike the other models, Yakopcic proposed the following equations for the dynamics of the state variable [32].

$$\frac{dx}{dt} = \eta \quad g(V(t)) f(x(t)) \tag{2}$$

$$g(V(t)) = \begin{cases} A_p(e^{V(t)} - e^{V_p}), & V(t) > V_p \\ -A_n(e^{-V(t)} - e^{V_n}), & V(t) < -V_n \\ 0, & -V_n \leqslant V(t) \leqslant V_p \end{cases} \tag{3}$$

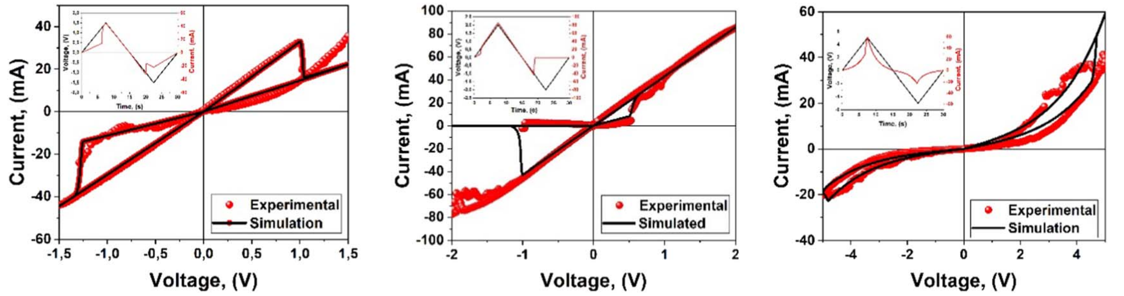

Figure 8. Simulation results of the generalized memristor model [32] adapted to the I–V characteristics profile of the memristive device of Si/SiO_2/Pt/TiO_x (t = 7.2 nm, 40 nm, 80 nm)/Pt. Inset figures show the applied voltage for 30 s and the calculated current. Solid red circle shows experimental data and the black line shows the fitting results.

$$f(x) = \begin{cases} e^{-\alpha_p(x-x_p)} \quad w_p(x, x_p), & x \geqslant x_p \\ 1, & x < x_p \end{cases} \tag{4}$$

$$f(x) = \begin{cases} e^{\alpha_n(x+x_n-1)} \quad w_n(x, x_n), & x \leqslant 1 - x_n \\ 1, & x > 1 - x_n \end{cases} \tag{5}$$

η is the polarity of the applied potential and it takes +1 or −1 depending on the direction of the current. The normalized state variable takes the value of 0 at the highest resistance value and 1 at the lowest resistance value, and directly determines the conductance of the memristor device. The state variable depends on two functions $g(V(t))$ and $f(x(t))$. The function $g(V(t))$ is entirely dependent on the application of a threshold voltage, and as long as the threshold voltage value is not exceeded, there is no change in the state variable. This dependence is clearly seen in many experimental data published in the literature [75–81]. In fact, this is the case for memristor devices with low ion mobility. Proposing two different threshold voltages in the negative and positive regions of the I-V curve provides an advantage in fitting the experimental curve. In addition, since the positive threshold voltage (V_p) and negative threshold voltage (V_n) values are constants within equation (3), each threshold value ensures that g(V(t)) starts from 0 when it is exceeded. The magnitude of the exponential terms (A_p and A_n) determines how fast the state changes when the threshold values are exceeded. The second function $f(x(t))$ provides nonlinear ion movement. While the state variable accelerates/slowdowns almost linearly in the middle regions of the memristor device, the movement of positively charged dopant ions or oxygen vacancies near the metal electrode is quite difficult (due to the electric field created by the charges accumulating at the boundary in the opposite direction to the applied electric field). Therefore, the function $f(x(t))$ ensures that the state variable does not change below certain threshold values but decreases exponentially by a factor of α_p and α_n when the boundary is reached. Like the threshold voltage, two different functions can be written for both positive and negative regions depending on the polarity of the applied voltage. The functions w_p and w_n in equations (4) and (5) are clearly window functions. When $x(t) = 1$, the state variable is guaranteed to be zero and x does not take negative values when the current direction changes.

$$w_p(x, x_p) = \frac{x_p - x}{1 - x_p} + 1 \tag{5a}$$

$$w_n(x, x_n) = \frac{x}{1 - x_n} \tag{6}$$

The generalized memristor model described above is a general model that physically includes the electron tunnel barrier, threshold voltage, and nonlinear drift model. The shape of the I-V curve is represented by the hyperbolic sine function, which is a result of the quantum tunneling effect in the MIM structure, called the 'Hyperbolic Sine Model' [30]. The TEAM model [29] ensures that there is no significant change in the memristor device's resistance without exceeding a certain threshold voltage. Finally, the 'Nonlinear Drift' [2] model is combined with the dynamics of the state variable, which is terminated when the device approaches its limits (minimum and maximum resistance state). The experimental I-V curve of the single cell memristor device in the form of Si/SiO_2/Pt/TiO_x/Pt given in figures 6(b)–(d) were simulated by using the generalized memristor model and the results are presented in figure 8 and table 4. In simulations, all devices were subjected to the triangular voltage during 30 s and the current was calculated by using equation (1). The physical meaning of the parameters is given in [32].

Table 4. Fitting parameters of the simulation of experimental current–voltage curves.

	Parameters						
$SiO_2/Pt/TiO_x/Pt$	a_1	V_p	A_p	x_p	α_p	b	x_o
	a_2	V_n	A_n	x_n	α_n		
TiO_x (7.2 nm)	0.9	1.25	50	0.51	1	0.033	0.38
	1.0	1.0	50	0.51	250		
TiO_x (40 nm)	1.3	0.5	50	0.51	1	0.033	0.38
	1.3	1.0	100	0.51	5		
TiO_x (80 nm)	0.007	4.5	0.1	0.9	1000	0.585	0.6
	0.003	4.8	1	0.01	12		

4. Conclusions

In conclusion, the structural characteristics of $SiO_2/Pt/TiO_x/Pt$ metal-insulator-metal (MIM) and $SiO_2/Pt/TiO_x/Mo$(wire) layered thin film have been investigated by XRR, XPS and PL techniques. X-ray photoelectron spectroscopy and the photoluminescence measurements confirmed to the Ti^{3+} and oxygen-related defects in the memristor device fabricated by using Pulsed Laser Deposition. Resistive switching properties of the devices with the TiOx layers of thickness of the 7.2 nm and 40 nm show bipolar digital switching behavior with the ratio of R_{OFF}/R_{ON} ~2 and 6 respectively. This type of switching behavior is applicable to random access memory. However, for the sample with the TiO_x layer thicknesses of 80 nm shows bipolar analog switching behavior related to the low vacancy concentration compared to the thickness of the whole sample. Simulation results of the experimental current–voltage curve of the devices are going to be used for the fabrication of next generation of the device with suitable parameters such as threshold voltage, low power consumption and low SET/RESET voltages.

Acknowledgments

This work was supported by the Scientific and Technical Research Council of Turkey (TUBITAK) through the project No: 121F390, and project No: 115F472. We are grateful to Prof R I Khaibullin for helpful discussions.

Bulat Z Rameev thanks the support of this study by Russian Science Foundation (project number 22-19-00712, https://rscf.ru/project/22-19-00712/).

Data availability statement

The data cannot be made publicly available upon publication because no suitable repository exists for hosting data in this field of study. The data that support the findings of this study are available upon reasonable request from the authors.

Author contributions

SK and BÖ conceived of the presented idea. SK developed the theory and performed the computations. BÖ, ÖK and GE verified the analytical methods. LA and GE carried out the Photoluminescence studies of the samples. BÖ and ÖK carried out the x-ray Reflectivity and x-ray photoelectron spectroscopy studies of the samples. BR supervised the findings of XRR, XPS and PL. Electrical measurements and theoretical model have been performed by BÖ and SK. All authors discussed the results and contributed to the to writing final manuscript.

Conflicts of interest

All authors declare that they have no conflicts of interest.

Data and code availability

All data produced by authors are presented in this manuscript and they are available in DOI.

Supplementary information

There is no any additional material omitted from the main body of the text.

Ethical approval

Ethical approval is not applicable, because this article does not contain any studies with human or animal subjects.

ORCID iDs

Bünyamin Özkal https://orcid.org/0000-0002-9964-9250
Sinan Kazan https://orcid.org/0000-0002-8183-5733
Özgül Karataş https://orcid.org/0000-0003-3848-5800
Lütfi Arda https://orcid.org/0000-0003-0722-3891

References

[1] Chua L 1971 Memristor the missing circuit element *IEEE Trans. Cir. Theory* **18** 507519
[2] Strukov D, Snider G S, Stewart D R and Williams R 2008 The missing memristor found *Nature* **453** 80–3
[3] Zhao H, Liu Z, Tang J, Gao B, Zhang Y, Qian H and Wu H 2022 Memristor-based signal processing for edge computing *Tsinghua Science and Technology* **27** 455–71
[4] Hamdioui S *et al* 2015 Memristor based computation-in-memory architecture for data-intensive applications *Proc. of the Conf. on Design, Automation and Test in Europe* 1718–25
[5] Ji X, Dong Z, Zhou G, Lai C S, Yan Y and Qi D 2021 Memristive system based image processing technology: a review and perspective *Electronics* **10** 3176
[6] Maheshwari S *et al* 2021 Design flow for hybrid CMOS/Memristor systems—II. Circuit schematics and layout *in IEEE Transactions on Circuits and Systems I: Regular Papers* **68** 4876–88
[7] Maheshwari S, Stathopoulos S, Wang J, Serb A, Pan Y, Leene L B, Papavassiliou C, Constandinou T G and Prodromakis T 2020 Hybrid CMOS/Memristor circuit design methodology *ArXiv, abs/2012.02267*
[8] Vishwakarma A, Ampadu K O, Huebner M, Vishvakarma S and Reichenbach M 2023 Memristor-based CMOS hybrid circuit design and analysis *Procedia Computer Science* **218** 563–73
[9] Chang M *et al* 2015 *Read circuits for resistive memory (ReRAM) and memristor-based nonvolatile Logics 20th Asia and South Pacific Design Automation Conf., ASP-DAC* 2015, 569–74
[10] Gale E 2014 TiO_2 -based memristors and ReRAM: materials, mechanisms and models (a review) *Semicond. Sci. Technol.* **29** 104004
[11] Zamarreno-Ramos C, Camunas-Mesa L A, Perez-Carrasco J A, Masquelier T, Serrano-Gotarredona T and Linares-Barranco B 2011 On spike-timing dependent plasticity, memristive devices and building a self-learning visual cortex *Front. in Neuormorphic Eng.* **5** 26 (1)–(20)
[12] Gale E M, de Lacy Costello B and Adamatzky A 2012 Observation and characterization of memristor current spikes and their application to neuromorphic computation *Numerical Analysis and Applied Mathematics ICNAAM 2012: Int. Conf. of Numerical Analysis and Applied Mathematics. AIP Conf. Proc.* 1479, 1898–901
[13] Jin X, Rast A, Galluppi F, Davies S and Furber S 2010 Implimenting spike-timing dependent plasticity on SpiNNiker neuromorphic hardware *Int. Joint Conf. on Neural Networks (IJCNN)* 1–8
[14] Gale E, de Lacy Costello B and Adamatzky A 2014 *Memristor Networks, chapter Spiking in Memristor Networks* (Cham: Springer) (https://doi.org/10.1007/978-3-319-02630-5_17)
[15] Howard D, Gale E, Bull L, De Lacy Costello B P J and Adamatzky A 2012 Evolution of plastic learning in spiking networks via memristive connections *IEEE Trans Evolutionary Computation* **16** 711–29
[16] Chua L O and Kang S 1976 Memristive device and systems *Proc. of IEEE* 64, 209–23
[17] Khalid M, Mukhtar S, Siddique M A M and Ahmed S F 2019 Memristor based full adder circuit for better performance *Trans. Electr. Electron. Mater* **20** 403–10
[18] Kim S U, Kim S H and Jang H W 2021 Competing memristors for brain-inspired computing *iScience* **24** 101889
[19] Wang S *et al* 2023 Memristor-based intelligent human-like neural computing *', Adv. Electron.Mater* **9** 2200877
[20] Ahn M, Park Y, Lee S H, Chae S, Lee J, Heron J T, Kioupakis E, Lu W and Phillips J 2021 Memristors Based on (Zr, Hf, Nb, Ta, Mo, W) High-Entropy Oxides *Adv. Electron. Mater.* **7** 2001258
[21] Lee S H, Moon J Y, Jeong Y, Lee J, Li X, Wu H and Lu W 2020 Quantitative, dynamic TaOx memristor/resistive random access memory model *ACS Appl. Electron. Mater* **2** 701–9
[22] Fan-Yi M, Shukai D, Lidan W, Xiao-Fang H and Zhe-Kang D 2015 An improved WOx memristor model with synapse characteristic analysis *Acta Phys. Sin.* **64** 148501
[23] Chakrabarti B K *et al* 2017 A multiply-add engine with monolithically integrated 3D memristor crossbar/CMOS hybrid circuit *Sci. Rep.* **7** 42429
[24] Yao P, Wu H, Gao B, Tang J, Zhang Q, Zhang W, Yang J and Qian H 2020 Fully hardware-implemented memristor convolutional neural network *Nature* **577** 641–6
[25] Strukov D B, Snider G L, Stewart D J and Williams R 2008 The missing Memristor found *Nature* **453** 80–3
[26] Joglekar Y N and Wolf S J 2009 The elusive memristor: properties of basic electrical circuits *Eur. J. Phys.* **30**
[27] Biolek Z, Biolek D and Biolkova V 2009 Spice model of memristor with nonlinear dopant drift *Radioengineering* **18** 210–4
[28] Prodromakis T, Peh B P, Papavassiliou C and Toumazou C 2011 A versatile memristor model with nonlinear dopant kinetics' *IEEE Trans. Electron Devices* **58** 3099–105

[29] Kvatinsky S, Friedman E G, Kolodny A and Weiser U 2013 TEAM: ThrEshold adaptive memristor model ’ *in IEEE Transactions on Circuits and Systems I: Regular Papers* **60** 211–21

[30] Bakar R A, Kamarozaman N S, Abdullah W a T W and Herman S H 2018 Modified hyperbolic sine model for titanium dioxide-based memristive thin films *IOP Conf. Ser.: Mater. Sci. Eng.* **341**

[31] Pickett M D, Strukov D B, Borghetti J, Yang J, Snider G L, Stewart D J and Williams R 2009 Switching dynamics in titanium dioxide memristive devices *J. Appl. Phys.* **106** 074508

[32] Yakopcic C 2014 Memristor device modeling and circuit design for read out integrated circuits, memory architectures, and neuromorphic systems *Doctor of Philosophy in Electrical Engineering* (University Of Dayton)

[33] Simmons J G 1963 Generalized formula for the electric tunnel effect between similar electrodes separated by a thin insulating film *J. Appl. Phys.* **34** 1793–803

[34] Kwon D *et al* 2010 Atomic structure of conducting nanofilaments in TiO_2 resistive switching memory *Nat. Nanotechnol.* **5** 148–53

[35] Choi B I *et al* 2005 Resistive switching mechanism of TiO_2 thin films grown by atomic-layer deposition *J. Appl. Phys.* **98** 0333715

[36] Yao J, Sun Z, Zhong L, Natelson D and Tour J M 2010 Resistive switches and memories from silicon oxide *Nano Lett.* **10** 4105–10

[37] Wu Y, Lee B and Wong H 2010 Al_2O_3-Based RRAM Using Atomic Layer Deposition (ALD) With 1-μA RESET Current *IEEE Electron Device Lett.* **31** 1449–51

[38] Rahaman S H, Lin Y, Lee H, Chen Y, Chen P, Chen W, Hsu C, Tsai K, Tsai M and Wang P 2017 The role of Ti buffer layer thickness on the resistive switching properties of hafnium oxide-based resistive switching memories *Langmuir* **33** 4654–65

[39] Han J and Meyyappan M 2011 Copper oxide resistive switching memory for e-textile *AIP Adv.* **1** 032162

[40] Chen A *et al* 2005 Non-volatile resistive switching for advanced memory applications *Tech. Dig. IEDM* 746–9

[41] Jousseaume V *et al* 2009 *IEEE Int. Interconnect Technology Conf. (Sapporo, Japan, 1–3 June 2009)* 41–3

[42] Baek I *et al* 2004 Highly scalable non-volatile resistive memory using simple binary oxide driven by asymmetric unipolar voltage pulses *Tech. Dig. IEDM* 587–90

[43] Gibbons J F and Beadle W 1964 Switching properties of thin NiO films *Solid-State Electron.* **7** 785–90

[44] Shih A Y, Zhou W, Qiu J, Yang H, Chen S S, Mi Z and Shih I 2010 Highly stable resistive switching on monocrystalline ZnO *Nanotechnology* **21** 125201

[45] Liu S, Wu N and Ignatiev A 2000 Electric-pulse-induced reversible resistance change effect in magnetoresistive films *Appl. Phy., Lett.* **76** 2749

[46] Beck A, Bednorz J G, Gerber C, Rossel C and Widmer D 2000 Reproducible switching effect in thin oxide films for memory applications *Appl. Phy., Lett.* **77** 139

[47] Watanabe Y, Bednorz J G, Bietsch A, Gerber C, Widmer D, Beck A and Wind S J 2001 Current-driven insulator–conductor transition and nonvolatile memory in chromium-doped $SrTiO_3$ single crystals *Appl. Phy., Lett.* **78** 3738

[48] Chua L 2011 Resistance switching memories memristors *Appl. Phys.*A **102** 765–83

[49] Kumar V, Tripathy S and Mathew J 2018 Memristor based random number generator: architectures and evaluation *Procedia Computer Science* **125** 576–83

[50] Balatti S, Ambrogio S, Xu H and Ielmini D 2015 True random number generation by variability of resistive switching in oxide-based devices *in IEEE Journal on Emerging and Selected Topics in Circuits and Systems* **5** 214–21

[51] Indiveri G, Linares-Barranco B, Legenstein R, Deligeorgis G and Prodromakis T 2013 Integration of nanoscale memristor synapses in neuromorphic computing architectures *Nanotechnology* **24** 384010

[52] Serrano-Gotarredona T, Masquelier T, Prodromakis T, Indiveri G and Linares-Barranco B 2013 STDP and STDP variations with memristors for spiking neuromorphic learning systems *Frontiers in Neuroscience* **7** 1–15

[53] Zamarre˜no-Ramos C, Camu˜nas-Mesa L A, P´erez-Carrasco J A, Masquelier T, Serrano-Gotarredona T and Linares-Barranco B 2011 On spike-timing-dependent-plasticity, memristive devices, and building a self-learning visual cortex *Frontiers in Neuroscience* **5** 1–15

[54] Zhou W, Wen S, Liu Y, Liu L, Liu X and Chen L Q 2023 Forgetting memristor based STDP learning circuit for neural networks *Neural Networks* **158** 293–304

[55] CasaXPS software 2022 *Copyright © 2022* (Casa Software Ltd)

[56] Henke B L, Gullikson E M and Davis J C 1993 X-Ray interactions: photoabsorption, scattering, transmission, and reflection at E = 50-30,000 eV, Z = 1-92 *Atom. Data Nucl. Data* **54** 181–342

[57] Bharti B, Kumar S, Lee H and Kumar R 2016 Formation of oxygen vacancies and Ti(3+) state in TiO2 thin film and enhanced optical properties by air plasma treatment *Sci Rep.* **6** 32355

[58] Babelon P, Dequiedt A, Mostéfa-Sba H, Bourgeois S, Sibillot P and Sacilotti M 1998 SEM and XPS studies of titanium dioxide thin films grown by MOCVD *Thin Solid Films* **322** 63–7

[59] Lin H, Rumaiz A K, Schulz M, Wang D, Rock R, Huang C P and Shah S I 2008 Photocatalytic activity of pulsed laser deposited TiO2 thin films *Materials Science and Engineering:* B **151** 133–9

[60] Dorcioman G, Fufa O, Craciun V, Miroiu M, Garoi P, Axente E, Sima F and Craciun D 2018 Investigations of thin titanium oxide films grown by reactive pulsed laser deposition *Romanian Journal of Oral Rehabilitation* **10** 41–9

[61] Luca D 2005 Preparation of tiox thin films by reactive pulsed-laser ablation *J. Optoelectron. Adv. Mater.* **7** 625–30

[62] Kawasaki H, Ohshima T, Yagyu Y, Ihara T, Tanaka Y and Suda Y 2015 Titaniun oxide thin film preparation by pulsed laser deposition method using Ti and TiO2 powder Target *Trans. Mat. Res. Soc. Japan* **40** 21–4

[63] Albu D F, Lungu J, Popescu-Pelin G, Mihăilescu C N, Socol G, Georgescu A, Socol M and Bănică A 2022 Victor ciupina and ion N. mihailescu, thin film fabrication by pulsed laser deposition from TiO2 targets in O2, N2, He, or Ar for dye-sensitized solar cells *Coatings* **12** 293

[64] Diebold U 2003 The surface science of titanium dioxide *Surf. Sci. Rep.* **48** 53–229

[65] Arenas-Hernandez A, Zúñiga-Islas C, Torres-Jacome A and Mendoza-Cervantes J C 2020 Self-organized and self-assembled TiO2 nanosheets and nanobowls on TiO2 nanocavities by electrochemical anodization and their properties *Nano Ex.* **1** 010054

[66] Xu M, Chen Y, Qin J, Feng Y, Li W, Chen W, Zhu J, Li H and Bian Z 2018 Unveiling the role of defects on oxygen activation and photodegradation of organic pollutants *Environ. Sci. Technol.* **52** 13879–86

[67] Liu F, Lu L, Xiao P, He H, Qiao L and Zhang Y 2012 Effect of oxygen vacancies on photocatalytic efficiency of TiO2 nanotubes aggregation *Bull. Korean Chem. Soc.* **33** 2255

[68] Rosales M, Zoltan T, Yadarola C, Mosquera E, Gracia F and García A 2019 The influence of the morphology of1D TiO2 nanostructures on photogeneration of reactive oxygen species and enhanced photocatalytic activity *J. Mol. Liq.* **281** 59–69

[69] Pandiyan R, Bartali R, Micheli V, Gottardi G, Luciu I, Ristic D, Goget G A, Ferrari M and Laidani N 2011 Influence of Nd3+ doping on the structural and near-IR photoluminescence properties of nanostructured TiO2 films *Energy Procedia* **10** 167–71

[70] Arenas-Hernandez A, Zúñiga-Islas C and Mendoza-Cervantes J C 2020 A study of the effect of morphology on the optical and electrical properties of TiO2 nanotubes for gas sensing applications *Eur. Phys. J. Appl. Phys.* **90** 30102

[71] Mathew S, Prasad A, Benoy T, Rakesh P P, Hari M, Libish T M, Radhakrishnan P, Nampoori V P N and Vallabhan C P G 2012 UV-Visible photoluminescence of TiO_2 nanoparticles prepared by hydrothermal method *Journal of Fluorescence* **22** 1563–9

[72] Ravidhas C, Anitha B, Arivukarasan D, Venkatesh R, Christy A J, Jothivenkatachalam K, Nithya A, Raj A T, Ravichandran K and Sanjeeviraja C 2016 Tunable morphology with selective faceted growth of visible light active TiO_2 thin films by facile hydrothermal method: structural, optical and photocatalytic properties *J Mater Sci: Mater Electron* **27** 5020–32

[73] Wojdyr M 2010 Fityk: a general-purpose peak fitting program *Journal of Applied Crystallography* **43** 1126–8

[74] Buckwell M, Ng H K, Mannion D J, Cox H R J, Hudziak S, Mehonic A and Kenyon A J 2021 Neuromorphic dynamics at the nanoscale in silicon suboxide RRAM *Front. Nanotechnol.* **3** 699037

[75] Oblea A S, Timilsina A, Moore D and Campbell K A 2010 Silver chalcogenide based memristor devices *The 2010 International Joint Conference on Neural Networks (IJCNN)* 1–3

[76] Jo S, Chang T, Ebong I, Bhadviya B, Mazumder P and Lu W 2010 Nanoscale memristor device as synapse in neuromorphic systems *Nano Lett.* **10** 1297–301

[77] Snider G S 2008 Cortical computing with memristive nanodevices *SciDAC Rev.* **10** 58–65

[78] Calado P, Gelmetti I, Hilton B, Azzouzi M, Nelson J and Barnes P R F 2021 Driftfusion: an open source code for simulating ordered semiconductor devices with mixed ionic-electronic conducting materials in one dimension *J. Comput. Electron.* **21** 960–91

[79] Liu P, Jia C and Zhang W 2022 Threshold switching memristor based on the BaTiO3/Nb:SrTiO3 epitaxial heterojunction for neuromorphic computing *ACS Appl. Electron. Mater* **4** 982–9

[80] Bae Y H, Lee A Y, Kwak J M, Im H and Hong J T 2011 Dependence of resistive switching behaviors on oxygen content of the $Pt/TiO_{2\text{-}x}/Pt$ matrix *Curr. Appl Phys.* **11** 66–9

[81] Oliveira F J, Cipriano R B, Da Silva F T B G, Romão E C and Santos C A M D 2020 Simple analytical method for determining electrical resistivity and sheet resistance using the van der Pauw procedure *Sci Rep.* **10** 16379